ACS Photonics

Article

pubs.acs.org/journal/apchd5

# Terahertz Radiation Imaging of Ferroelectric Domain Topography in Room-Temperature Hydrogen-Bonded Supramolecular Ferroelectrics

Masato Sotome,[†] Noriaki Kida,[*,†] Sachio Horiuchi,[‡,§] and Hiroshi Okamoto[†]

[†]Department of Advanced Materials Science, The University of Tokyo, 5-1-5 Kashiwa-no-ha, Chiba 277-8561, Japan

[‡]National Institute of Advanced Industrial Science and Technology (AIST), Tsukuba 305-8562, Japan

[§]CREST, Japan Science and Technology Agency (JST), Tokyo 102-0075, Japan

Supporting Information

**ABSTRACT:** We report quasi-three-dimensional imaging of the ferroelectric domains in a hydrogen-bonded supramolecular ferroelectric 1:1 salt of 5,5′-dimethyl-2,2′-bipyridine and deuterated iodanilic acid by mapping out terahertz waves radiated from the crystal upon femtosecond laser irradiation. Polarization dependence of the effective depth radiating the terahertz waves due to the absorption anisotropy for terahertz waves allows us to distinguish domains in the inside and surface regions of the crystals. In an as-grown crystal, a large domain covering almost all the area is discerned in the inside region, while multidomains are discerned in the surface regions. We observed polarization switching via domain boundary motion in the direction perpendicular to the direction of hydrogen-bonded chains in the surface regions under an external electric field. Obtained images suggest that an uncharged 180° domain wall (DW) parallel to the stacking plane of hydrogen-bonded chains covers the whole area at coercive fields. We argue that the DW dynamics stems from the anisotropic crystal structure, i.e., stacking of hydrogen-bonded chains.

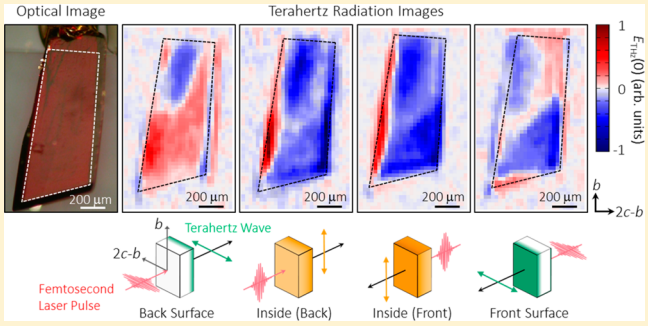


**KEYWORDS:** *organic ferroelectrics, terahertz radiation imaging, ferroelectric domains, nonlinear optical properties*

In ferroelectrics, polarization switching by external electric fields proceeds by propagation of ferroelectric domain walls (DWs), which separate ferroelectric domains with different polarizations.[1−4] Such a polarization switching process and the subsequent re-formation of ferroelectric domains are the basis for ferroelectric devices such as nonvolatile memories.[1,3,4] Thus, understanding of ferroelectric DW dynamics is needed for the development of the devices using ferroelectric materials. Ferroelectric domain topography and DW dynamics are determined by the symmetry of the crystal,[2,5,6] but in reality they are governed by various factors such as the depolarization field at the surface,[7−9] size,[10] and growth conditions,[2,6] resulting in unpredictable complex patterns of ferroelectric domains and DWs.[2,11−13] DWs are roughly classified into two types in terms of relative angle between the electric polarization $P$ and DW,[14] i.e., uncharged (neutral) DWs parallel to $P$ and charged DWs perpendicular to $P$. Since uncharged DWs are electrically stable (div$P$ = 0), they are observed in various ferroelectrics.[2] On the other hand, originally unstable charged DWs such as head-to-head (tail-to-tail) DWs frequently appear in as-grown crystals[15−18] and as-grown thin films[19−21] and have net bound charge (div$P \neq 0$), which should be compensated by charged objects such as free carriers, defects, and impurities. Therefore, real-space imaging of ferroelectric domain topography is indispensable to understand the nature of ferroelectricity and thus crucial for the applications of ferroelectric materials. Great research activities have therefore developed various methods for visualization of ferroelectric domains.[22] Examples are X-ray topography,[23] scanning electron microscopy,[24] piezoelectric force microscopy (PFM),[25] electro-optic imaging microscopy,[26] Raman confocal microscopy,[27] second-harmonic-generation microscopy (SHG),[28,29] near-field scanning optical microscopy,[30] and emission of terahertz waves.[31−33]

Recently, a new series of room-temperature hydrogen-bonded ferroelectrics with large ferroelectric polarization have been developed in a family of low-dimensional organic molecular crystals.[34−36] Molecules in these crystals are connected by hydrogen bonds; cooperative proton transfer along with the asymmetric $\pi$-electron conjugation change induces ferroelectric polarization. Compared to inorganic ferroelectrics, organic ferroelectrics have advantages in light-weight, flexible, low-cost, and environmentally benign characteristics. Thus, they are now receiving great research attention in terms of new room-temperature electronic and photonic

**Received:** June 26, 2015
**Published:** August 5, 2015





DOI: 10.1021/acsphotonics.5b00351
*ACS Photonics* 2015, 2, 1373−1383

applications. In the context of these applications, the detection of ferroelectric domain topography is indispensable. Recent works on a croconic acid (4.5-dihydroxy-4-cyclopentene-1,2,3-trion)[32] and [H-6,6′-dmbp][Hca] (6,6′-dimethyl-2,2′-bipyridinium chloranilate),[37] both of which are room-temperature hydrogen-bonded ferroelectrics, have revealed the presence of charged head-to-head (tail-to-tail) DWs in the virgin state of as-grown crystals. The charged DWs diminish in electrically poled crystals[32] or thermally annealed crystals.[37] In the study of a croconic acid,[32] ferroelectric domain topography was detected by mapping out the amplitude of terahertz waves radiated from the crystal upon the irradiation of femtosecond laser pulses. Since the thickness or depth inside the crystal contributing to the terahertz wave radiated outside the crystal was large (~600 $\mu$m), the terahertz radiation image obtained in a 100-$\mu$m-thick sample reflects bulk ferroelectric domains. In the study of [H-6,6′-dmbp][Hca], on the other hand, PFM was used to detect the ferroelectric domain topography.[37] In general, domain topography is different in the surface and inside regions of the crystal. PFM detects ferroelectric domains in the surface, while the terahertz radiation imaging method applied on croconic acid[32] detects bulk ferroelectric domains. In order to further reveal the characteristics of the ferroelectric domain topography in organic ferroelectrics, it is necessary to develop a method that can distinguish orientations of ferroelectric domains in the inside and surface regions. Generally, detected depth in nonlinear optical methods depends on the absorption of fundamental and/or generated light. In fact, estimation of the three-dimensional domain topography of domains has been reported for antiferromagnetic 180° domains in $LiCoPO_4$ and $LiNiPO_4$ by utilizing frequency dependence of the penetration length of SHG.[38] Terahertz radiation imaging based on the optical rectification effect is also expected to be able to reveal three-dimensional domain topography, provided that the sample has frequency- or polarization-dependent absorption in the terahertz frequency region.

Here, we propose a method to visualize ferroelectric domains and DWs in the inside and surface regions of organic ferroelectrics and applied this method to an organic molecular crystal, the 1:1 salt of 5,5′-dimethyl-2,2′-bipyridine (55DMBP) and deuterium iodanilic acid ($D_2$ia) ([D-55DMBP][Dia]), which was recently found to be a room-temperature ferroelectric.[39] We show that a terahertz wave is emitted by the irradiation of a femtosecond laser pulse, and the effective depth radiating the terahertz waves exhibits large polarization dependence. By mapping out the electric field amplitude of two orthogonally polarized terahertz waves, we successfully visualize distinct ferroelectric domains in the inside and surface regions of the crystal. In the inside region of an as-grown crystal, an almost single domain is discerned, while a multidomain is observed in the surface region. The polarization switching by an external electric field can be explained by the motion of uncharged one-dimensional (1D) interchain domain boundaries within stacking layers of hydrogen-bonded chains. This results in the formation of an interlayer 2D 180° DW almost parallel to the stacking plane. On the basis of systematic optical measurements in the terahertz and visible frequency regions, we discuss DW dynamics and principles of the present terahertz radiation imaging technique.

[D-55DMBP][Dia] investigated here is the deuterated analogue of the 1:1 salt of 55DMBP and $H_2$ia ([H-55DMBP][Hia]) with a Curie temperature $T_c$ = 268 K.[39] The crystal structure of [H-55DMBP][Hia] is triclinic with the space group $P1$ and $P\bar{1}$ in the ferroelectric and paraelectric phases, respectively. 55DMBP and $H_2$ia molecules arrange alternately to form one-dimensional hydrogen-bonded chains parallel to the $2c-b$ axis, as shown in Figure 1. Protons in the

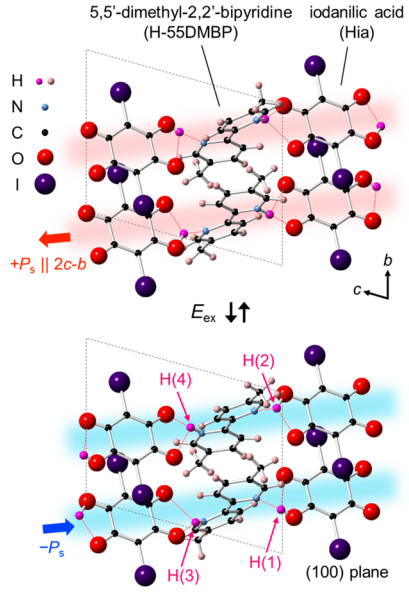


**Figure 1.** Schematic illustration of the crystal structure of [H-55DMBP][Hia] in the ferroelectric phase (50 K). The dashed parallelogram indicates the unit cell. Spontaneous polarization ($P_s$) shows up along the $2c-b$ axis, and polarization switching is induced by the application of an external electric field ($E_{ex}$).

intermolecular hydrogen bonds are located at off-center positions, which is accompanied by asymmetric $\pi$-electron distribution and thus induces electric polarization along the hydrogen-bonded chain axis, i.e., the $2c-b$ axis.[39] The positions of the protons can be switched by an external electric field (Figure 1), resulting in the polarization reversal. A notable characteristic of [H-55DMBP][Hia] is the deuterium effect on the ferroelectric properties; the deuterated single crystal, [D-55DMBP][Dia], shows the spontaneous polarization $P_s$ of ~2 $\mu$C/cm$^2$ even at room temperature ($T_c$ = 335 K).[39] In this work, we focused on [D-55DMBP][Dia].

## RESULTS AND DISCUSSION

**Polarized Optical Spectra in Terahertz and Visible Frequency Regions.** First, we show the results of the polarized reflectance $R$ and transmittance $T$ spectra in the energy range of 0.7−5.0 eV. $R$ spectra obtained with the electric field of light $E$ parallel to the $b$ axis ($E \parallel b$) and $2c-b$ axis ($E \parallel 2c-b$) are shown in the right panel of Figure 2a by orange and green solid lines, respectively. No remarkable anisotropy is observed. In both polarizations, strong peak structures are discerned at ~3.8 eV, assigned to intramolecular electronic excitations, i.e., $\pi-\pi^*$ transitions of the molecules. We also show in Figure 2a polarized $T$ spectra by orange and green dotted lines. The steep decrease of $T$ above 1.7 eV is due to the presence of $\pi-\pi^*$ transitions. We performed the Kramers−Kronig transformation of $R$ spectra to extract the refractive index $n$ spectra in $E \parallel b$ and $E \parallel 2c-b$ configurations, which are shown in Figure 2b. The $n$ spectra in the energy range 1.0−2.0 eV were reproduced by the Sellmeier relationship, which is represented by $n = [1 + (S_0\lambda_0^2/(1 - (\lambda_0/\lambda)^2))]^{1/2}$, where $\lambda$ is


DOI: 10.1021/acsphotonics.5b00351
ACS Photonics 2015, 2, 1373−1383

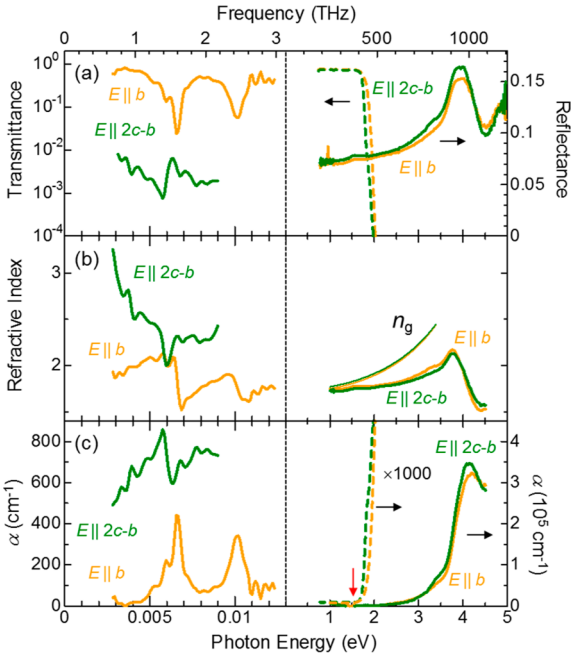


**Figure 2.** Polarized optical spectra of [D-55DMBP][Dia] for $E \parallel 2c-b$ (green lines) and $E \parallel b$ (orange lines) in terahertz and visible frequency regions, measured at room temperature. (a) Transmittance and reflectance, (b) refractive index, and (c) absorption coefficient $\alpha$ spectra. We also show in (b) the group refractive index $n_g$ spectrum derived from the Sellmeier relationship. Dotted lines in (c) were calculated from the transmittance spectra (vertically expanded by a factor of 1000). Solid lines in the visible frequency region of (c) were obtained by the Kramers–Kronig transformation of the reflectance spectra. The red downward arrow in (c) indicates the photon energy of the femtosecond laser pulse (1.55 eV) used in terahertz radiation experiments.

the wavelength. This yields $S_0 = 5.17 \times 10^{-5}$ nm$^{-2}$ and $\lambda_0 = 193$ nm for $E \parallel b$, while $S_0 = 5.53 \times 10^{-5}$ nm$^{-2}$ and $\lambda_0 = 190$ nm for $E \parallel 2c-b$. With the use of the obtained fitting parameters, we estimated the group refractive index $n_g$ spectra, where $n_g = |n - \lambda(dn/d\lambda)|$, as shown in Figure 2b. There is little anisotropy of $n_g$ at 1.55 eV (the photon energy of the femtosecond laser pulses in this study), which was evaluated to be ∼1.8 for both configurations. Figure 2c shows the absorption coefficient $\alpha$ spectra; solid lines were obtained by the Kramers–Kronig transformation of the $R$ spectra, while dotted lines were derived from the relation $\alpha = -(1/d)\ \ln(T/(1-R)^2)$ with $d$ the thickness of the sample ($d$ = 0.15 mm). $\alpha$ at 1.55 eV was estimated to be ∼10 cm$^{-1}$, which corresponds to a penetration depth of ∼1 mm for the femtosecond laser pulses in terahertz radiation experiments.

In the left panel of Figure 2a, we show the polarized transmittance $T$ spectra in the terahertz frequency region in $E \parallel b$ and $E \parallel 2c-b$ configurations. The measured frequency ranges in $E \parallel b$ and $E \parallel 2c-b$ configurations were 0.7–3.0 and 0.7–2.2 THz, respectively. In contrast to $T$ spectra in the visible frequency region, there is a large anisotropy; $T$ at 1.0 THz in the $E \parallel 2c-b$ configuration is ∼100 times smaller than that in the $E \parallel b$ configuration. In the $E \parallel b$ configuration, we identify peak structures at ∼1.6 and ∼2.4 THz, which would be assigned to intramolecular or intermolecular vibrations. On the other hand, broad absorption in the measured frequency region (0.7–2.2 THz) is discerned in the $E \parallel 2c-b$ configuration. From the measured $T$ spectra, we extracted $n$ and $\alpha$ spectra, which are shown in Figure 2b and c, respectively. Details of our derivation procedure are described in ref 40. $n$ in the $E \parallel 2c-b$ configuration increases with lower frequency, while $n$ in the $E \parallel b$ configuration shows the dispersion of multiple Lorentz oscillators. Accordingly, a relatively large $\alpha$ in the $E \parallel 2c-b$ configuration is discerned over the whole measured frequency range. This broad absorption was previously reported in the related analogue [H-55DMBP][Hia] by far-infrared reflectivity measurements;[41] its origin was discussed in terms of the enhancement of the proton fluctuation.

**Terahertz Radiation.** In terahertz radiation experiments, we used a 240-$\mu$m-thick (100)-oriented single crystal. Since the penetration depth (∼1 mm) of the incident femtosecond laser pulses exceeds the thickness of the sample, attenuation of the laser pulse inside the sample is negligible. External electric fields $E_{ex}$ = ±5 kV/cm, which exceed the coercive field (∼2 kV/cm),[39] were applied along the $2c-b$ axis. The electric fields of the femtosecond laser pulses $E^{\omega}$ and the detected terahertz waves $E_{THz}$ were set parallel to the $2c-b$ axis, i.e., $E^{\omega} \parallel 2c-b$ and $E_{THz} \parallel 2c-b$. Figure 3a shows the terahertz electric field

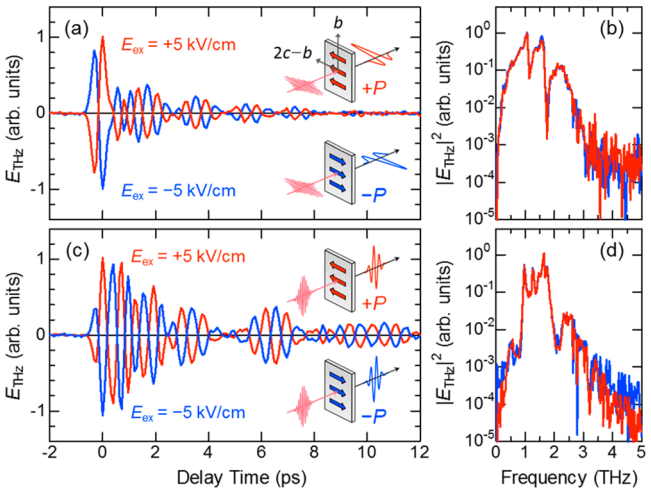


**Figure 3.** (a) Electric-field waveforms emitted from [D-55DMBP][Dia] in $E^{\omega} \parallel 2c-b$ and $E_{THz} \parallel 2c-b$ configurations, measured at room temperature. We applied an external electric field $E_{ex}$ of ±5 kV/cm, which exceeds the coercive field (∼2 kV/cm). (b) Fourier-transformed power spectra. (c) Electric field waveforms and (d) power spectrum in $E^{\omega} \parallel b$ and $E_{THz} \parallel b$ configurations. Insets in (a) and (c) show schematic illustrations of the optical configurations with respect to crystal orientation. Electric polarization $P$ is represented by the arrow.

waveforms $E_{THz}(t)$ radiated from the crystal. A nearly single-cycle pulse around 0 ps is discerned in a time window from −0.6 to 0.4 ps, and subsequent temporal oscillation components emerge up to ∼8 ps. We observed reversal of the terahertz waveform when the sign of $E_{ex}$ was changed. As detailed below, this is caused by a polarization switching (the inset of Figure 3a). To see the spectra of the terahertz wave, we performed fast Fourier transformation (FFT) on the measured waveforms, the results of which are shown in Figure 3b. They contain frequency components up to 3 THz and have two dip structures at around 1.2 and 1.7 THz. The origins of these dip structures are unclear at present, since a broad absorption in the $E \parallel 2c-b$ configuration obscures other spectral features such as optical phonons (Figure 2c).

We also observed emission of terahertz waves in the $E^{\omega} \parallel b$ and $E_{THz} \parallel b$ configuration; typical terahertz electric field


DOI: 10.1021/acsphotonics.5b00351
ACS Photonics 2015, 2, 1373–1383

waveforms with $E_{ex}$ = ±5 kV/cm and their FFT spectra are shown in Figure 3c and d, respectively. The electric field at 0 ps in this configuration (Figure 3c) is slightly (1%) larger than that in the $E^{\omega} \parallel 2c-b$ and $E_{THz} \parallel 2c-b$ configurations (Figure 3a). The spectral width of the terahertz waveform is narrower than that obtained in the $E^{\omega} \parallel 2c-b$ and $E_{THz} \parallel 2c-b$ configurations, and the temporal oscillation component is more pronounced, which appears as peaks in the frequency range 1−2 THz (Figure 3d). It was also found that the phase of the radiated terahertz waves is sensitive to the direction of the ferroelectric polarization, as illustrated in the inset of Figure 3c.

So far, various optical processes have been proposed as the terahertz radiation mechanism in non-centrosymmetric media.[42] In room-temperature hydrogen-bonded organic ferroelectrics such as croconic acid[32] and 2-phenylmalondialdehyde,[43] the terahertz radiation mechanism is optical rectification of the incident laser pulse by a second-order nonlinear optical process.[44] Terahertz radiation mechanisms related to photocarrier generation can be ignored for [D-55DMBP][Dia], since it is transparent to the near-infrared femtosecond laser pulse. Thus, possible terahertz radiation mechanisms are optical rectification[44] and/or coherent phonon generation by impulsive stimulated Raman scattering;[40,45] both processes can be described by the second-order nonlinear optical coefficient tensor $\chi^{(2)}_{ijk}$. A laser-induced nonlinear polarization $P^{NL}$ is given by

$$P_i^{NL} = \epsilon_0 \chi^{(2)}_{ijk} E_j^{\omega} E_k^{\omega *} \tag{1}$$

where $\epsilon_0$ is the vacuum permittivity. All the $\chi^{(2)}_{ijk}$ components are allowed in the space group $P1$.

To reveal the role of the second-order nonlinear optical effects on the emission of terahertz waves, we measured the laser polarization and power dependences. Figure 4a shows a schematic illustration of the experimental setup for the measurement of the laser polarization dependence. We used a 240-$\mu$m-thick (100)-oriented single crystal in this experiment. A single-domain state was obtained by application of $E_{ex}$ = 5 kV/cm along the $2c-b$ axis. The laser power was set to be 10 mW. We rotated the polarization of the incident femtosecond laser pulses by the angle $\theta$ with a half-wave plate; $\theta$ was defined as the angle of the laser polarization relative to the $X$ axis. We measured terahertz waveforms $E_{+45°}(t)$ and $E_{-45°}(t)$ by setting the WG1 angle at +45° and −45°, respectively. Terahertz waveforms of the horizontal ($X \parallel 2c-b$) component $E_X(t)$ and vertical ($Y \parallel b$) component $E_Y(t)$ were obtained from $E_{+45°}(t)$ and $E_{-45°}(t)$ by the relation

$$E_X(t) = \frac{1}{2}(E_{+45°}(t) + E_{-45°}(t)) \tag{2}$$

$$E_Y(t) = \frac{1}{2}(E_{+45°}(t) - E_{-45°}(t)) \tag{3}$$

Amplitude spectra of the waveforms $E_X(\omega)$ and $E_Y(\omega)$ were obtained by FFT of $E_X(t)$ and $E_Y(t)$, respectively. When the light-induced nonlinear polarization given by eq 1 is dominant in the terahertz radiation process, power spectra of the terahertz waves $|E_i(\omega)|^2$ ($i$ = $X$, $Y$) in terms of $\theta$ are given by

$$\begin{aligned} |E_i(\omega)|^2 \propto [&\chi^{(2)}_{iXX}(\omega)\cos^2\theta + (\chi^{(2)}_{iYX}(\omega) + \chi^{(2)}_{iXY}(\omega))\cos\theta \\ &\times \sin\theta + \chi^{(2)}_{iYY}(\omega)\sin^2\theta]^2 \\ &\times I_0^2 L_{gen}^2(\omega) T'(\omega) \end{aligned} \tag{4}$$

where $I_0$ is the incident laser power, $L_{gen}$ is the effective generation length,[40,46] and $T'(\omega) = 4n^2/((n+1)^2 + \kappa^2)$ is the transmittance of the terahertz waves at the sample−air interface with $\kappa$ the extinction coefficient. $L_{gen}$ represents the effective length of the region contributing to the observed terahertz waves; $L_{gen}$ is given by

$$L_{gen}(\omega) = \left( \frac{1 + \exp(-\alpha(\omega)d) - 2\exp\left(-\frac{\alpha(\omega)}{2}d\right)\cos\left(\frac{\omega}{c}|n(\omega) - n_g|d\right)}{\left(\frac{\alpha(\omega)}{2}\right)^2 + \left(\frac{\omega}{c}\right)^2 (n(\omega) - n_g)^2} \right)^{1/2} \tag{5}$$

where $c$ is the speed of light in a vacuum.

Here, $|E_i(\omega)|^2$ was integrated in the frequency range 0.8−1.2 THz, where the terahertz radiation is relatively strong for both polarizations (Figure 3b and d). $T$ values in $E_{THz} \parallel 2c-b$ and $E_{THz} \parallel b$ configurations were 0.68 and 0.89, respectively. $L_{gen}$ values of the 240-$\mu$m-thick crystal were 28 $\mu$m ($E_{THz} \parallel 2c-b$) and 205 $\mu$m ($E_{THz} \parallel b$). Figure 4b shows the measured $\theta$ dependence of $|E_i(\omega)|^2$. Equation 4 reproduces the measured $\theta$ dependence of $|E_i(\omega)|^2$, as indicated by solid lines in Figure 4b. The resultant ratios of $\chi^{(2)}_{ijk}$ components to $\chi^{(2)}_{YYY}$ are as follows: $\chi^{(2)}_{XXX}/\chi^{(2)}_{YYY} = -8.3$, $\chi^{(2)}_{XYY}/\chi^{(2)}_{YYY} = 5.3$, $\chi^{(2)}_{YXX}/\chi^{(2)}_{YYY} = -0.7$, $(\chi^{(2)}_{YYX} + \chi^{(2)}_{YXY})/\chi^{(2)}_{YYY} = -0.7$, and $(\chi^{(2)}_{XYX} + \chi^{(2)}_{XXY})/\chi^{(2)}_{YYY} = 5.1$. We show in Figure 4c the laser power dependence of $|E_X(\omega)|^2$ and $|E_Y(\omega)|^2$ in the $E^{\omega} \parallel 2c-b$ configuration, which is also well reproduced by eq 4 (solid lines in Figure 4c). These results indicate that terahertz radiation in [D-55DMBP][Dia] is induced by a second-order nonlinear optical process. Since sharp dip structures, which may be related to the phonon modes, are observed in the power spectra of the terahertz radiation (Figure 3b and d), comprehensive Raman scattering experiments are needed to further discuss the terahertz radiation mechanism. Here, we focus on the ferroelectric domain imaging using emission of terahertz waves.

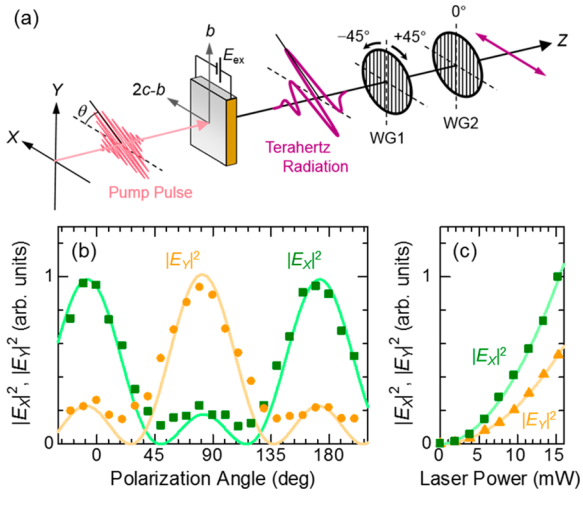


**Figure 4.** (a) Schematic illustration of the experimental setup. We used two wire grids (WGs); the angle of WG1 was set to 45° or −45° with respect to the $Y$-direction. An external electric field $E_{ex}$ = +5 kV/cm was applied. (b) Laser polarization dependence of the intensity of the terahertz waves $|E_{THz}|^2$ in the frequency range 0.8−1.2 THz. Solid lines are least-squares fittings by eq 4. (c) Laser power dependence of $|E_{THz}|^2$ with $\theta$ = 0°. Solid lines are quadratic fitting curves.



DOI: 10.1021/acsphotonics.5b00351
ACS Photonics 2015, 2, 1373−1383

**Ferroelectric Domain Imaging Using Emission of Terahertz Waves.** In order to visualize ferroelectric domains and DWs,[5] various methods have been developed so far. Among them, optical means were widely used to detect ferroelectric domains over a wide area of the sample.[2] Using emission of terahertz waves, spatial distributions of ferroelectric domains and DWs have been visualized in various ferroelectrics such as $BiFeO_3$ thin film,[31] $Co_3B_7O_{13}I$,[33] and croconic acid.[32] It was found that the phase of the terahertz wave radiated from ferroelectric materials upon irradiation of a femtosecond laser pulse depends on the direction of the ferroelectric polarization. Thus, ferroelectric domains with different polarizations can be easily distinguished by mapping out the amplitude of the radiated terahertz waves over the sample. This method was recently applied to visualize ferroelectric domains with different polarizations in croconic acid[32] and $Co_3B_7O_{13}I$.[33] In croconic acid, tail-to-tail and 180° domains were successfully detected in as-grown and electrically poled crystals, respectively.[32] On the other hand, a 90° domain was discerned in $Co_3B_7O_{13}I$.[33] In previous studies on croconic acid[32] and $Co_3B_7O_{13}I$,[33] we mapped out the electric field of the terahertz wave polarized only along the ferroelectric polarization direction. Since the detected signal of ferroelectric domains along the depth direction is averaged, we were not able to detect a three-dimensional ferroelectric domain and DWs in the crystals.

On the other hand, a notable feature of the terahertz radiation in [D-55DMBP][Dia] is that two orthogonally polarized terahertz waves can be generated (Figure 3). In addition, this compound is optically anisotropic and the absorption coefficient along $2c-b$ is much larger than along $b$ in the terahertz frequency region (Figure 2). This makes us expect that different parts in the depth direction contribute to the radiated terahertz waves with the two polarization directions $E_{THz} \parallel 2c-b$ and $E_{THz} \parallel b$. Using this, we will be able to evaluate the depth profiles of the contributions to the radiated terahertz wave and therefore obtain information on the direction of the ferroelectric polarization. The amplitude spectrum $E_{THz}(\omega,d)$ of the terahertz wave at the far point outside the crystal is given by

$$E_{THz}(\omega, d) = H(\omega)\frac{\mu_0\chi^{(2)}(\omega)\,\omega^2 I(\omega)}{n_o\left\{\frac{c}{\omega}\left[\frac{\alpha(\omega)}{2}+\alpha_o\right]+i[n(\omega)+n_g]\right\}} \times \frac{\exp\left[-\frac{i\omega n(\omega)}{c}d\right]\exp\left[-\frac{\alpha(\omega)}{2}d\right]-\exp\left[-\frac{i\omega n_g}{c}d\right]\exp[-\alpha_o d]}{\frac{\alpha(\omega)}{2}-\alpha_o+\frac{i\omega}{c}[n(\omega)-n_g]} \quad (5)$$

where $\mu_0$ is the magnetic permeability in a vacuum, $\omega_0$ is the central angular frequency of the femtosecond laser pulse (800 nm ~375 THz), $\alpha_0$ is the absorption coefficient at $\omega_0$ (~9 $cm^{-1}$ for $E_{THz} \parallel 2c-b$ and ~8 $cm^{-1}$ for $E_{THz} \parallel b$), $n_0$ is the refractive index at $\omega_0$ (~1.78 for $E_{THz} \parallel 2c-b$ and ~1.75 for $E_{THz} \parallel b$), and $I(\omega)$ is the Fourier-transformed intensity spectrum of the femtosecond laser pulse.[40,46] Here, $H(\omega)$ is detection response function of the LT-GaAs detector used in our experiments, as detailed in ref 40. We derived $\chi^{(2)}$ spectra in the $E_{THz} \parallel 2c-b$ and $E_{THz} \parallel b$ configurations from eq 5 using FFT amplitude spectra of the terahertz waves shown in Figure 3a and c, respectively. Frequency-dependent contribution $G(\omega,z)$ of the terahertz waves generated at depth $z$ to the observed $E_{THz}(\omega,d)$ is given by

$$G(\omega, z) = \chi^{(2)}(\omega)\,E_{Inst}(\omega)\exp\left[-\frac{i\omega n_g}{c}z\right]\exp[-\alpha_o z] \times \exp\left[-\frac{i\omega n(\omega)}{c}(d-z)\right]\exp\left[-\frac{\alpha(\omega)}{2}(d-z)\right] \quad (6)$$

where $E_{Inst}(\omega) = \omega^2 H(\omega) I(\omega)$ is the instrumental function in our experimental setup, as detailed in ref 40. Here, we focus on the electric field of the terahertz waveform at 0 ps. Thus, spectrally integrated $G(\omega,z)$ gives the depth profile of the contribution to the detected terahertz wave $G(z)$, which is given by

$$G(z) = \mathrm{Re}\{\int_{\omega_1}^{\omega_2} d\omega G(\omega, z)/\int_{\omega_1}^{\omega_2} d\omega G(\omega, d)\} \quad (7)$$

Since the back surface region mainly contributes to $E_{THz}(0)$, we divided $\int_{\omega_1}^{\omega_2} d\omega G(\omega,z)$ by $\int_{\omega_1}^{\omega_2} d\omega G(\omega,d)$. We obtained polarized $T$ spectra in the frequency range 0.8−2.2 THz and 0.8−3.0 THz in $E_{THz} \parallel 2c-b$ and $E_{THz} \parallel b$ configurations, respectively (Figure 2a). Thus, we set $\omega_1/2\pi$ and $\omega_2/2\pi$ the lowest and highest values of the measured frequency range, respectively. The calculated $G(z)$ profiles in the $E_{THz} \parallel 2c-b$ and $E_{THz} \parallel b$ configurations with $d$ = 150 $\mu$m are shown in Figure 5a and b, respectively. We defined the effective depth $L_{eff}$

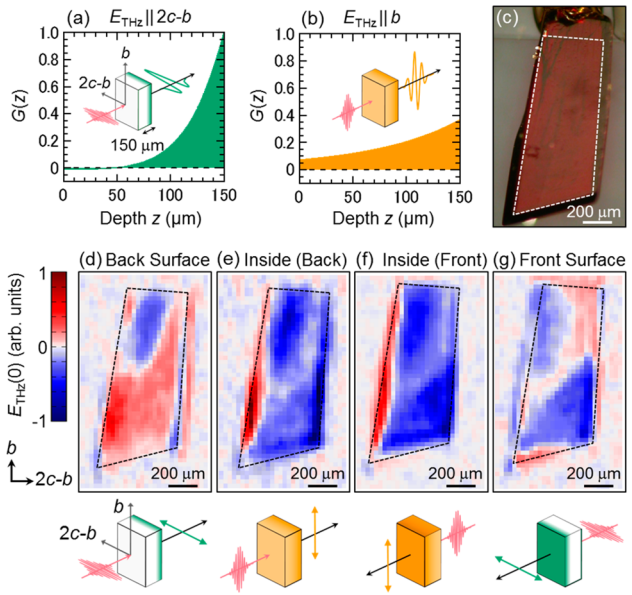


**Figure 5.** (a) Depth profile of the terahertz radiation $G(z)$ in $E^{\omega} \parallel 2c-b$ and $E_{THz} \parallel 2c-b$ configurations with a sample thickness $d$ of 150 $\mu$m. (b) $G(z)$ in $E^{\omega} \parallel b$ and $E_{THz} \parallel b$ configurations. $G(z)$ is normalized to give the same area in (a) and (b). Insets in (a) and (b) show the optical configurations. The areas colored with green and yellow indicate regions radiating the terahertz waves in the optical configurations shown in (a) and (b), respectively. (c) Optical microscope image. (d−g) Terahertz radiation images in the optical configurations depicted below. Dashed areas in (c−g) indicate the valid area of the terahertz radiation images.

as the length from the back surface where $G(z)$ becomes $1/e$ of $G(d)$. In the $E_{THz} \parallel 2c-b$ configuration, $L_{eff}$ was estimated to be ~29 $\mu$m. This indicates that the back side region of the crystal with a depth of ~29 $\mu$m mainly contributes to the detected terahertz waves, as schematically shown in the inset of Figure 5a. On the other hand, $L_{eff}$ in the $E_{THz} \parallel b$ configuration reaches ~89 $\mu$m. Thus, terahertz waves generated from the inside region of the crystal are detected (inset of Figure 5b).



DOI: 10.1021/acsphotonics.5b00351
ACS Photonics 2015, 2, 1373−1383

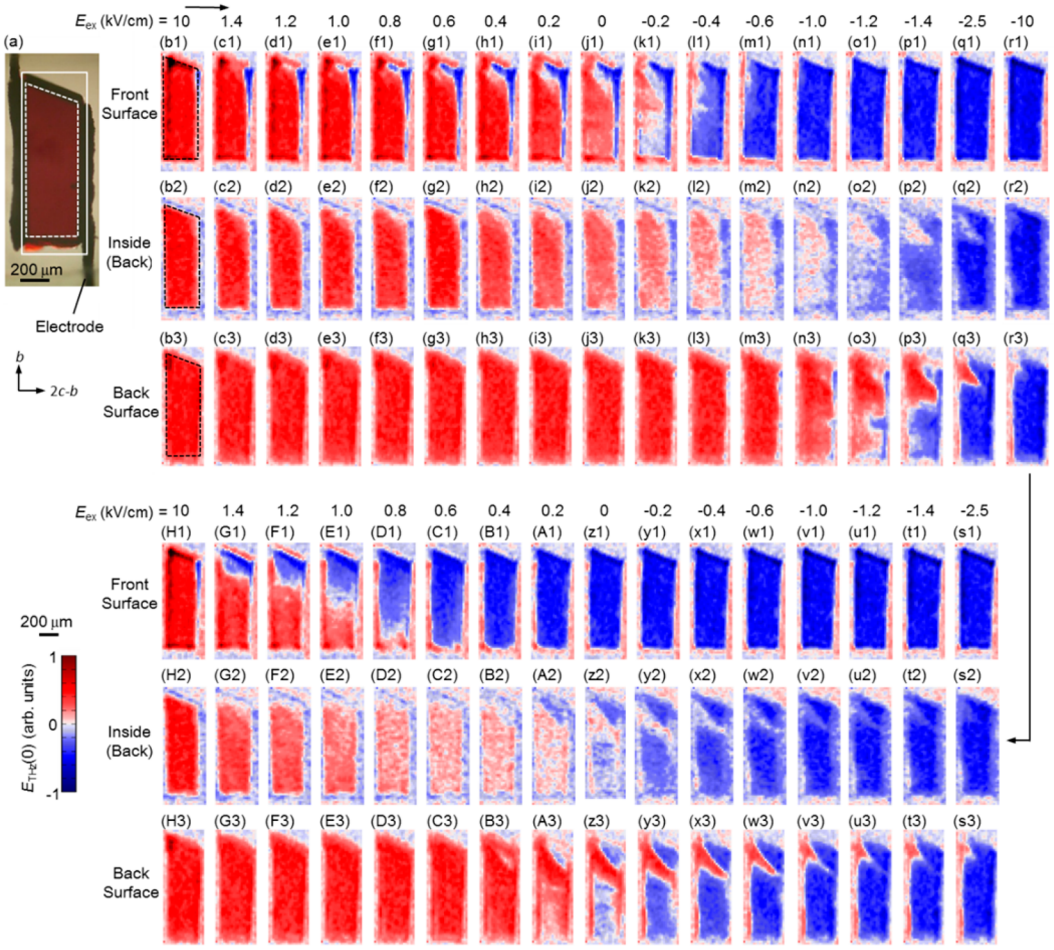


**Figure 6.** (a) Optical microscope image. (b-H) Terahertz radiation images in (1) front surface, (2) inside, and (3) back surface regions under electric fields. First, we applied the electric field $E_{ex}$ of 10 kV/cm exceeding the coercive field (~2 kV/cm) and measured terahertz radiation images in (b). As guided by arrows, $E_{ex}$ (kV/cm) was changed as 10 → 0 → −10 → 0 → 10. During this procedure, terahertz radiation images were taken as shown in (c) to (H). The plus direction of $E_{ex}$ is from left to right. Full data are compiled in the Supplemental Movie.

In the terahertz imaging experiments, we measured the electric field of the terahertz wave at 0 ps $[E_{THz}(0)]$ at various positions of an as-grown crystal by a raster scan. The spot diameter of the incident femtosecond laser pulse, which corresponds to the spatial resolution of the terahertz radiation images, was ~25 $\mu$m. This experiment is conducted on a 150-$\mu$m-thick (100)-oriented as-grown crystal. First, we adopt the configuration shown in the lower part of Figure 5d, in which the crystal is irradiated with a femtosecond laser pulse from the front side, and $E^{\omega}$ and $E_{THz}$ were parallel to the $2c-b$ axis. In this configuration, ferroelectric domains in the back surface region (~29 $\mu$m) can be visualized, since $L_{eff}$ is ~29 $\mu$m (Figure 5a). The upper panel of Figure 5d shows the terahertz radiation image of the crystal. The optical microscope image of the same area is shown in Figure 5c. Although the crystal has a wide (100)-oriented flat surface, edge areas are not normal to the (100)-surface, as seen in Figure 5c; the flat region of the crystal and thus the actual valid area of the terahertz radiation image are surrounded by the dotted lines. The color scale shown in the left-hand side of Figure 5d represents the magnitude and sign of $E_{THz}(0)$. The red and blue regions indicate that the sign of $E_{THz}(0)$ is different. Thus, these regions correspond to ferroelectric domains with opposite polarization directions, i.e., $P_s \parallel \pm(2c-b)$. In the white region, $E_{THz}(0)$ is nearly zero, which corresponds to the ferroelectric DWs. Since the width of each white region is almost equal to the spatial resolution (~25 $\mu$m), the actual DW width is narrower than ~25 $\mu$m. From this image, we can see that ferroelectric domains with sizes larger than ~200 $\mu$m exist in the back surface region of ~29 $\mu$m. These domains are separated by two types of DWs: uncharged 180° DWs with a plane parallel to the $\pm(2c-b)$ axis and charged head-to-head (or tail-to-tail) DWs with a plane perpendicular to the $\pm(2c-b)$ axis. In addition, we discern the presence of inclined DWs.

To reveal the ferroelectric nature inside the crystal, we measured the terahertz radiation image in the $E_{THz} \parallel b$ configuration, which is shown in Figure 5e. Since the terahertz radiation efficiencies in $E_{THz} \parallel 2c-b$ (Figure 5d) and $E_{THz} \parallel b$ (Figure 5e) configurations are different, it is necessary to correct the value of $E_{THz}(0)$ for $E_{THz} \parallel b$. In the case of the 240-$\mu$m-thick crystal, $E_{THz}(0)$ for $E_{THz} \parallel b$ is found to be slightly (1%) larger than that for $E_{THz} \parallel 2c-b$ (Figure 3a and c). The $d$ dependence of $E_{THz}(0)$ is given by $\int_0^d dzG(z)$. Compared to the 240-$\mu$m-thick crystal, $\int_0^d dzG(z)$ of the 150-$\mu$m-thick crystal is 105% and 84% in the $E_{THz} \parallel 2c-b$ and $E_{THz} \parallel b$ configurations, respectively. Thus, $E_{THz}(0)$ in the $E_{THz} \parallel b$ configuration was multiplied by $1.24 = 1.05/(0.84 \times 1.01)$ as the correction of the anisotropy in the terahertz radiation efficiency. In the $E_{THz} \parallel b$ configuration, ferroelectric domains inside the crystal can be visualized, since $L_{eff}$ is ~89 $\mu$m (Figure 5b). Compared to the


DOI: 10.1021/acsphotonics.5b00351
ACS Photonics 2015, 2, 1373−1383

ferroelectric domain image shown in Figure 5d, different patterns of ferroelectric domains are observed in Figure 5e. The crystal consists of ferroelectric domains with opposite polarizations, a large blue-colored domain and a small red-colored domain, which are separated by a head-to-head (or tail-to-tail) DW. Note that the lower region of the crystal is occupied by the blue-colored domain, although the same area in the back surface region consists of the red-colored domain (Figure 5d). This indicates the presence of a quasi-2D 180° DW along the (100) plane in the lower region of the crystal. We also performed a similar experiment by reversing the crystal along the $b$ axis. Namely, the crystal is irradiated with a femtosecond laser pulse from the back side, as illustrated in the lower part of Figure 5f. The obtained terahertz radiation image is shown in the upper panel of Figure 5f. The ferroelectric domain image is similar to that shown in Figure 5e. This ensures that the terahertz radiation images obtained in the $E_{THz} \parallel b$ configurations reflect the bulk ferroelectric domains.

Figure 5g shows the terahertz radiation image of the front surface region of the crystal measured in the $E_{THz} \parallel 2c-b$ configuration and with a femtosecond laser pulse incident from the back side. As can be seen, the observed multidomain structure is different from the images in the back surface and inside regions (Figure 5d, e, and f). The ferroelectric domain indicated by the red region can be seen as white regions in the bulk ferroelectric domain images shown in Figure 5e and f. The comparison of four terahertz radiation images clearly indicates that ferroelectric domains are not uniform in the depth direction and DWs are easily introduced in surface regions of the crystal.

Here, we briefly discuss the possible reason that such a ferroelectric multidomain state appears in as-grown crystals. Single crystals of [D-55DMBP][Dia] were prepared by recrystallization at room temperature,[39] which is lower than $T_c$ = 335 K. Thus, ferroelectric domain patterns are mainly determined by the kinetics of the crystal growth. In general, charged (head-to-head or tail-to-tail) DWs are electrically unstable,[2] so that the presence of charged DWs is attributed to the existence of charged impurities and/or defects during the crystal growth. These impurities and defects can compensate electrical charges of DWs, resulting in ferroelectric multidomain states. In the case of croconic acid, charged tail-to-tail DWs are discerned only in the virgin state of as-grown crystals and diminish by cyclic application of electric fields,[32] which may be explained by the removal of DW pinning by external electric fields.

So far, various methods were used to observe ferroelectric domains and DWs. The most important advantage of the terahertz radiation imaging is that orientations of ferroelectric domains can be determined by phase information on terahertz waves, which is very sensitive to the direction of ferroelectric polarizations. In the present work, we successfully visualized ferroelectric domains and DWs in the inside and surface regions of as-grown crystals by using the anisotropy of the optical properties in the terahertz frequency regions. In organic molecular ferroelectrics, collective modes show up along the direction of the ferroelectric polarization,[41,47] resulting in the large optical anisotropy in the terahertz frequency region. Thus, the present method is not restricted to [D-55DMBP][Dia] but can be applied to a variety of organic ferroelectrics with optical anisotropy in the terahertz frequency region. In addition, terahertz radiation imaging is a nondestructive and contact-free method. This feature enables us to easily detect ferroelectric domain topography and DW dynamics under external electric fields.

**Ferroelectric Domain Dynamics under External Electric Field.** In this section, we discuss ferroelectric domain dynamics under external electric fields. In this experiment, we used another as-grown crystal. The thickness of the sample was 150 $\mu$m. An optical image of the sample with two electrodes is shown in Figure 6a. Terahertz radiation images were taken in the area indicated by the solid white box; the actual area available for the ferroelectric domain imaging is surrounded by the dotted while lines. First, $E_{ex}$ = 10 kV/cm, which exceeds the coercive field (~2 kV/cm),[39] was applied along the $2c-b$ axis in order to make the crystal a single domain. We measured three terahertz radiation images in the front surface region with ~29 $\mu$m, the inside region, and the back surface region with ~29 $\mu$m, which are shown in Figure 6(b1), (b2), and (b3), respectively. As can be seen in the figure, the crystal is occupied with a single domain with almost uniform polarization, except for the right upper region (indicated in blue) in the front surface. We show in Figure 6 variation of the domain pattern when $E_{ex}$ (kV/cm) was changed as 10 → 0 → −10 → 0 → 10. Full domain images are compiled in the Supporting Information. At $E_{ex}$ = 1.0 kV/cm, a ferroelectric domain with a size of ~100 $\mu$m (indicated in blue) is generated in the upper part of the front surface region, as shown in Figure 6(e1). On the other hand, the single-domain state is preserved in the inside and back surface regions, which can be seen in Figure 6(e2) and (e3), respectively. Further decreasing $E_{ex}$, the ferroelectric domain initially generated in the front surface region grows in size [Figure 6(f1)] and merges into another ferroelectric domain located at the right-hand side of the crystal [Figure 6(g1)]. When $E_{ex}$ is decreased to zero, the red-colored domain is preserved in the inside and back surface regions, which are discerned in Figure 6(j2) and (j3), respectively. These results clearly indicate the appearance of the blue-colored ferroelectric domain is limited within the front surface region. By applying negative $E_{ex}$, polarization switching proceeds as follows. First, an additional ferroelectric domain indicated in blue is generated in the front surface region [Figure 6(k1)] with uncharged 180° DWs. These DWs move along the $b$ axis and diminish the original red-colored ferroelectric domain [Figure 6(l1)]. By taking into account the anisotropy of intralayer and interlayer electrostatic interactions of molecular layers, as is discussed later in detail, these DWs are probably quasi-1D in each molecular layer parallel to the (100) plane. In the back surface region, on the other hand, the original ferroelectric domain is unchanged [Figure 6(l3)]. Thus, the uncharged 180° DWs are generated and move only in the front region. The magnitude of the terahertz radiation generated inside the crystal is near zero in all areas of the crystal [Figure 6(l2)] compared to that in $E_{ex}$ = +10 kV/cm [Figure 6(b2)]. This can be explained by the destructive interference of the terahertz waves radiated in the opposite ferroelectric domains in the front and back halves. In other words, an uncharged 2D 180° DW probably almost parallel to the sample surface, i.e., the (100) plane, is generated; the uncharged 2D 180° DW divides the crystal into two ferroelectric domains with opposite polarizations in the depth direction. The signs of $E_{THz}(0)$ are different in the front and back surface regions [Figure 6(m1) and (m3)], but their magnitudes are almost identical. This indicates that this uncharged 2D 180° DW locates the middle region of the crystal, as illustrated in Figure 7(c2). At $E_{ex}$ = −0.6 kV/cm, the front surface region is occupied with a single



DOI: 10.1021/acsphotonics.5b00351
ACS Photonics 2015, 2, 1373−1383

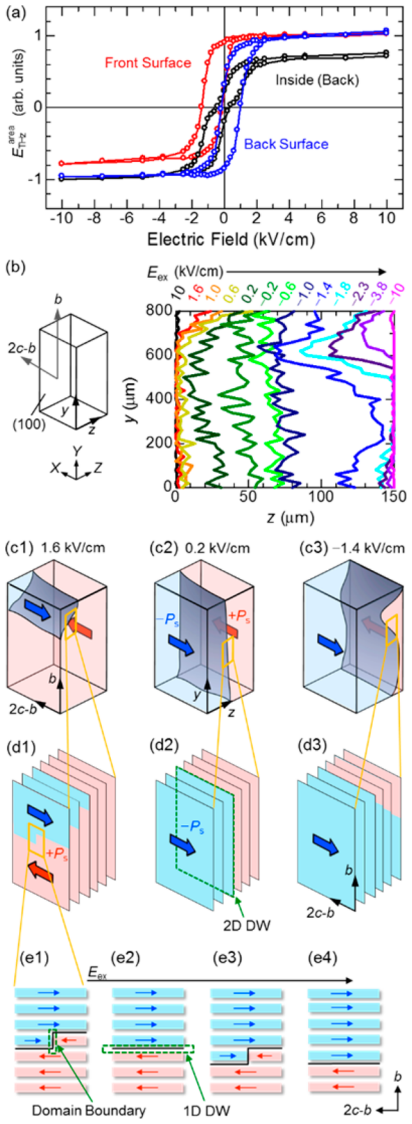


**Figure 7.** (a) Electric field dependence of the total amplitude of the images in the front surface, inside, and back surface regions in Figure 6. (b) Estimated DW depth on the $Y$−$Z$ plane in 10 kV/cm → −10 kV/cm. $X$, $Y$, and $Z$ axes relative to crystal orientations are schematically shown. Schematic illustrations are focused on (c) DWs and (d) molecular stacking. The 2D DW is surrounded by the dotted line in (d2). (e) Microscopic interpretation of the ferroelectric polarization switching process under electric fields. Domain boundary and 1D DWs are surrounded by dotted lines.

domain [Figure 6(m1)]. With further increasing $|E_{ex}|$, a portion of the red-colored domains inside the crystal becomes smaller than that of the blue-colored domains [Figure 6(o2) and (p2)], whereas the red-colored domain in the back surface region is almost preserved. At $E_{ex}$ = −1.2 kV/cm, an uncharged 180° DW and a charged head-to-head (or tail-to-tail) DW are generated in the back surface region [Figure 6(o3) and (p3)]. Finally, the charged head-to-head (or tail-to-tail) DW disappears and a pair of the uncharged 180° DWs proceeds along the $b$ axis, resulting in the blue-colored single-domain state [Figure 6(r3)].

When $E_{ex}$ (kV/cm) was further changed as −10 → 0 → 10, the overall behavior of the ferroelectric domains [Figure 6(r1) to (H1)] are almost opposite of that in the $E_{ex}$ (kV/cm) scan (10 → 0 → −10). In this process, oblique 180° DWs first appear in the back surface region [Figure 6(s3) to (y3)] and propagate along the $b$ axis. At 0.6 kV/cm, the red-colored single-domain state is realized in the back surface region [Figure 6(C3)], whereas the blue-colored domain is preserved in the front surface region [Figure 6(C1)]. The wide white-colored region is observed inside the crystal [Figure 6C(2)], indicating the presence of an uncharged 2D 180° DW almost parallel to the (100) plane. With increasing $E_{ex}$, the magnitude of the red-colored domain increases inside the crystal [Figure 6(D2)] and the uncharged 180° DW shows up in the front surface region [Figure 6(D1)]. Finally, the uncharged 180° DW moves along the $b$ axis, resulting in the red-colored single domain in the whole volume [Figure 6(H1) to (H3)].

To clearly see the domain switching in response to $E_{ex}$, we show in Figure 7a the $E_{ex}$ dependence of the total amplitude of the terahertz radiation, $E_{THz}^{area}$, obtained by the integration of $E_{THz}(0)$ over the entire crystal area in the $E_{ex}$ (kV/cm) scan (10 → 0 → −10 → 0 → 10); the red, black, and blue circles indicate $E_{THz}^{area}$ in the front surface, inside, and back surface regions. $E_{THz}^{area}$ from the inside of the crystal shows a hysteresis loop, reflecting the bulk ferroelectric nature. Furthermore, two kinks can be discerned at around ±0.5 kV/cm. Compared to $E_{THz}^{area}$ in the inside region, the hysteresis loops of $E_{THz}^{area}$ in the front and back surface regions are shifted by ∼0.6 kV/cm in the opposite direction. Namely, the coercive field of the front surface region is different from that of the back surface region. The hysteresis loop of $E_{THz}^{area}$ in the inside images shows a steep increase or decrease at the coercive fields of front and back regions. This implies that DW motion in the each half rules the domain switching behavior.

In order to discuss the stability of the DW under $E_{ex}$, we estimate the position of a DW along the depth direction, i.e., the $Z$-direction, using terahertz radiation images in the front, inside, and back surface regions (Figure 6); $X$-, $Y$-, and $Z$-directions relative to crystal orientations are illustrated on the left side of Figure 7b. The crystal becomes single-domain states under $E_{ex}$ = ±10 kV/cm [Figure 6(b), (r), and (H)], while the crystal is divided into two domains by an uncharged 2D 180° DW under $E_{ex}$ = −0.6 kV/cm [Figure 6(m)] and $E_{ex}$ = 0.6 kV/cm [Figure 6(C)]. This allows us to assume only one domain boundary in the depth direction; the DW depth is 0 and 150 μm under $E_{ex}$ = +10 kV/cm and $E_{ex}$ = −10 kV/cm, respectively. Under this assumption, $E_{THz}(0)$ in the terahertz radiation images in the inside [Figure 6(b2)−(r2)] normalized by that in $E_{ex}$ = +10 kV/cm [Figure 6(r2)] correspond to the DW depth $z$; $z$ is estimated by the relation $E_{THz}(0) = -\int_0^z G(z')\,dz' + \int_z^d G(z')\,dz'$. The DW was projected on the $Y$−$Z$ plane by averaging $z$ in the $X$-direction (∥ 2$c$−$b$) for simplicity. Figure 7(b) shows the $E_{ex}$ dependence of the DW depth when $E_{ex}$ was changed as +10 → 0 → −10; $z$ = 0 μm and $z$ = 150 μm correspond to positions of the front and back surfaces, respectively. At $E_{ex}$ = 1.6 kV, a DW shows up in the upper region of the front surface region, as discerned by the red line in Figure 7b. The DW is not flat but tilted in the $Y$−$Z$ plane. Figure 7(c1) shows the schematic illustration of the prospected position of the DW (indicated by the gray area); arrows indicate the direction of the ferroelectric polarization. At $E_{ex}$ = −0.2 kV/cm, the position of DW locates at $z \approx 70$ μm and the DW became flat, as indicated by the green line in Figure 7b. This corresponds to the completion of domain switching in the front half as schematically shown in Figure 7(c2). In the back half, a tilted DW appears again at $E_{ex}$ = −1.4 kV/cm (the blue line in Figure 7b), the schematic illustration of which is shown


DOI: 10.1021/acsphotonics.5b00351
ACS Photonics 2015, 2, 1373−1383

in Figure 7(c3). With increasing $|E_{ex}|$, the tilted DW in the upper region finally diminishes at $E_{ex} = -10$ kV/cm, which may be related to the Barkhausen pulses frequently observed in ferroelectrics.[1,48]

By taking into account the anisotropy of intralayer and interlayer electrostatic interactions of the molecular layers, we briefly discuss the reason that polarization switching proceeds with successive propagations of uncharged 180° DW along the $b$ axis (Figure 6), and an uncharged 2D 180° DW almost parallel to the (100) plane is finally formed (Figure 7c). [D-5SDMBP][Dia] is formed by hydrogen-bonded chain layers in the (100) plane and their stacking along the direction perpendicular to the (100) plane, which are schematically shown in Figure 7d. The precise structural data of [D-5SDMBP][Dia] is not available. Thus, we used X-ray structural data of the related analogue [H-5SDMBP][Hia] at 50 K in the ferroelectric phase[39] to deduce the anisotropy in intralayer and interlayer electrostatic interactions. Protons in the ferroelectric phase occupy four crystallographically nonequivalent sites within hydrogen-bonded chain plane, which are labeled by H(1), H(2), H(3), and H(4) in Figure 1. The H(1)−H(2) and H(3)−H(4) distances were estimated to be ∼4.148 and ∼5.989 Å, respectively, which are much shorter than the distance (∼8.725 Å) between the neighboring layers. Thus, interlayer electrostatic interaction along the stacking direction, i.e., perpendicular to the (100) plane, should be weak, compared to intralayer electrostatic interaction. This causes the formation of uncharged interchain 1D domain boundaries within the hydrogen-bonded chain layers. By the application of $E_{ex}$ along the $2c-b$ axis, transfer of protons within the hydrogen-bonded chain occurs so that an intrachain domain boundary [the dotted line in Figure 7(e1)] separated by a head-to-head (or tail-to-tail) polarization is displaced along the $2c-b$ axis [Figures 7(e1) and (e2)]. Subsequently, the interchain domain boundary [the dotted line in Figure 7(e2)] moves along the $b$ axis [Figure 7(e3) and (e4)], which is consistent with the observed DW dynamics (Figure 6). This process results in the formation of an interlayer 180° DW under nearly zero electric fields [the dotted line in Figure 7(d2)], which agrees well with the observation of the uncharged 2D 180° DW almost parallel to the (100) plane. However, the actual DW is stabilized by subtle competition between intralayer and interlayer electrostatic interactions so that the actual domain topography may be influenced by the presence of pinning centers such as defects induced during the crystal growth. This would be the main origin of the tilted DW schematically shown in Figure 7(c1) and (c3).

## CONCLUSION

We successfully visualized the ferroelectric domain topography of a room-temperature hydrogen-bonded supramolecular ferroelectric [D-5SDMBP][Dia] by terahertz radiation imaging. Using the anisotropy in the effective depth of the region contributing to the terahertz waves, we developed a new method to detect the ferroelectric domains and DWs in the inside and surface regions of the as-grown crystal. Application of the external electric field along the $2c-b$ axis caused the generation of an uncharged 2D 180° DW almost parallel to the (100) plane. The domain switching process is explained by the propagation of the uncharged interchain 1D domain boundaries along the $b$ axis. This new method presented here can be applied to quasi-three-dimensional visualization of ferroelectric domains and DWs in other organic ferroelectrics with optical anisotropy in the terahertz frequency region.

## METHODS

The (100)-oriented single crystals of [D-5SDMBP][Dia] were obtained by recrystallization from a solution. Details of the sample preparation were reported elsewhere.[39]

Polarized transmittance spectra in the terahertz frequency region were measured by the standard terahertz time-domain spectroscopy.[42] We used a 0.5-mm-thick (110)-oriented ZnTe single crystal as a terahertz wave emitter and photoconducting switch on a low-temperature-grown GaAs substrate as a detector. A 0.15-mm-thick (100)-oriented single crystal of [D-5SDMBP][Dia] was attached on a circular aperture with a diameter of 1 mm made of copper.

We measured polarized transmittance and reflectance spectra in the energy range of 0.7−5.0 eV by a grating spectrometer.

In the terahertz radiation experiments, femtosecond laser pulses delivered from a mode-locked Ti:sapphire laser (a wavelength of 800 nm, a repetition rate of 80 MHz, and a pulse width of 100 fs) were focused on a sample in normal incidence.[32,42] Unless otherwise stated, laser power was set to be 5 mW. The laser spot diameter was estimated to be ∼25 $\mu$m on the sample surface; thus the laser energy density is 25 $\mu$J/cm$^2$ per pulse. We employed a photoconductive sampling technique to measure the electric field waveform of the radiated terahertz waves.[42] Two wire grid polarizers (WG1, WG2) were used to confine the detected polarization of the radiated terahertz waves. A pair of electrodes with conducting carbon paste was attached on the side (102) surfaces of a crystal so as to apply the electric field along the $2c-b$ axis.

All the experiments were performed at room temperature.

## ASSOCIATED CONTENT

### Supporting Information

The Supporting Information is available free of charge on the ACS Publications website at DOI: 10.1021/acsphotonics.5b00351.

Movie of ferroelectric domain dynamics under external electric field (AVI)

## AUTHOR INFORMATION

### Corresponding Author

*E-mail: kida@k.u-tokyo.ac.jp.

### Notes

The authors declare no competing financial interest.

## ACKNOWLEDGMENTS

This work was partly supported by a Grant-in-Aid by MEXT (No. 25247049, 25600072, 15H03549, and No. 25-3372). M.S. was supported by Japan Society for the Promotion of Science (JSPS) through Program for Leading Graduate Schools (MERIT) and JSPS Research Fellowships for Young Scientists.

## REFERENCES

(1) Lines, M. E.; Glass, A. M. *Principles and Applications of Ferroelectrics and Related Materials*; Oxford University Press, 1977.
(2) Tagantsev, A. K.; Cross, L. E.; Fousek, J. *Domains in Ferroic Crystals and Thin Films*; Springer: New York, 2010.
(3) Scott, J. F. *Ferroelectric Memories*; Springer: New York, 2000.
(4) Catalan, G.; Seidel, J.; Ramesh, R.; Scott, J. F. Domain Wall Nanoelectronics. *Rev. Mod. Phys.* **2012**, *84*, 119−156.
(5) Fousek, J.; Janovec, V. The Orientation of Domain Walls in Twinned Ferroelectric Crystals. *J. Appl. Phys.* **1969**, *40*, 135−142.



DOI: 10.1021/acsphotonics.5b00351
*ACS Photonics* 2015, 2, 1373−1383

(6) Dvorak, V.; Janovec, V. Angular Energy Dependence of a 180° Domain Wall in $BaTiO_3$. *Jpn. J. Appl. Phys.* **1965**, *4*, 400−402.
(7) Shin, Y.-H.; Grinberg, I.; Chen, I.-W.; Rappe, A. M. Nucleation and Growth Mechanism of Ferroelectric Domain-wall Motion. *Nature* **2007**, *449*, 881−884.
(8) Wang, Y. G.; Zhong, W. L.; Zhang, P. L. Surface and Size Effects on Ferroelectric Films with Domain Structures. *Phys. Rev. B: Condens. Matter Mater. Phys.* **1995**, *51*, 5311−5314.
(9) Prosandeev, S.; Bellaiche, L. Asymmetric Screening of the Depolarizing Field in a Ferroelectric Thin Film. *Phys. Rev. B: Condens. Matter Mater. Phys.* **2007**, *75*, 172109-1−4.
(10) Catalan, G.; Schilling, A.; Scott, J. F.; Gregg, J. M. Domains in Three-Dimensional Ferroelectric Nanostructures: Theory and Experiment. *J. Phys.: Condens. Matter* **2007**, *19*, 132201-1−7.
(11) Gregg, J. M. Exotic Domain States in Ferroelectrics: Searching for Vortices and Skyrmions. *Ferroelectrics* **2012**, *433*, 74−87.
(12) Lukyanchuk, I.; Sharma, P.; Nakajima, T.; Okamura, S.; Scott, J. F.; Gruverman, A. High-symmetry Polarization Domains in Low-symmetry Ferroelectrics. *Nano Lett.* **2014**, *14*, 6931−6935.
(13) Prosandeev, S.; Bellaiche, L. Characteristics and Signatures of Dipole Vortices in Ferroelectric Nanodots: First-Principles-Based Simulations and Analytical Expressions. *Phys. Rev. B: Condens. Matter Mater. Phys.* **2007**, *75*, 094102−1−9.
(14) Gureev, M. Y.; Tagantsev, A. K.; Setter, N. Head-to-Head and Tail-to-Tail 180° Domain Walls in an Isolated Ferroelectric. *Phys. Rev. B: Condens. Matter Mater. Phys.* **2011**, *83*, 184104-1−18.
(15) Shur, V. Ya; Rumyantsev, E. L.; Subbotin, A. L. Forming of the Domain Structure in Lead Germanate During Phase Transition. *Ferroelectrics* **1993**, *140*, 305−312.
(16) Gopalan, V.; Mitchell, T. E.; Furukawa, Y.; Kitamura, K. The Role of Nonstoichiometry in 180° Domain Switching of $LiNbO_3$ Crystals. *Appl. Phys. Lett.* **1998**, *72*, 1981−1983.
(17) Kitamura, K.; Furukawa, Y.; Niwa, K.; Gopalan, V.; Mitchell, T. E. Crystal Growth and Low Coercive Field 180° Domain Switching Characteristics of Stoichiometric $LiTaO_3$. *Appl. Phys. Lett.* **1998**, *73*, 3073−3075.
(18) Schröder, M.; Hauβmann, A.; Thiessen, A.; Soergel, E.; Woike, T.; Eng, L. M. Conducting Domain Walls in Lithium Niobate Single Crystals. *Adv. Funct. Mater.* **2012**, *22*, 3936−3944.
(19) Jia, C.-L.; Mi, S.-B.; Urban, K.; Vrejoiu, I.; Alexe, M.; Hesse, D. Atomic-scale Study of Electric Dipoles Near Charged and Uncharged Domain Walls in Ferroelectric Films. *Nat. Mater.* **2008**, *7*, 57−61.
(20) Seidel, J.; Martin, L. W.; He, Q.; Zhan, Q.; Chu, Y.-H.; Rother, A.; Hawkridge, M. E.; Maksymovych, P.; Yu, P.; Gajek, M.; Balke, N.; Kalinin, S. V.; Gemming, S.; Wang, F.; Catalan, G.; Scott, J. F.; Spaldin, N. A.; Orenstein, J.; Ramesh, R. Conduction at Domain Walls in Oxide Multiferroics. *Nat. Mater.* **2009**, *8*, 229−234.
(21) Guyonnet, J.; Gaponenko, I.; Gariglio, S.; Paruch, P. Conduction at Domain Walls in Insulating $Pb(Zr_{0.2}Ti_{0.8})O_3$ Thin Films. *Adv. Mater.* **2011**, *23*, 5377−5381.
(22) Soergel, E. Visualization of Ferroelectric Domains in Bulk Single Crystals. *Appl. Phys. B: Lasers Opt.* **2005**, *81*, 729−752.
(23) Canut, M.; Hosemann, R. X-ray Analysis of Ferroelectric Domains in the Paraelectric Phase of $NaNO_2$. *Acta Crystallogr.* **1964**, *17*, 973−981.
(24) Le Bihan, R. Study of Ferroelectric and Ferroelastic Domain Structures by Scanning Electron Microscopy. *Ferroelectrics* **1989**, *97*, 19−46.
(25) Kalinin, S. V.; Gruverman, A. *Scanning Probe Microscopy of Functional Materials*; Springer: Berlin, 2011.
(26) Gopalan, V.; Mitchell, T. E. *in situ* Video Observation of 180° Domain Switching in $LiTaO_3$ by Electro-optic Imaging Microscopy. *J. Appl. Phys.* **1999**, *85*, 2304−2311.
(27) Shur, V. Y.; Zelenovskiy, P. S.; Nebogatikov, M. S.; Alikin, D. O.; Sarmanova, M. F.; Ievlev, A. V.; Mingaliev, E. A.; Kuznetsov, D. K. Investigation of the Nanodomain Structure Formation by Piezoelectric Force Microscopy and Raman Confocal Microscopy in $LiNbO_3$ and $LiTaO_3$ Crystals. *J. Appl. Phys.* **2011**, *110*, 052013-1−6.
(28) Florsheimer, M.; Paschotta, R.; Kubitscheck, U.; Brillert, C.; Hofmann, D.; Heuer, L.; Schreiber, G.; Verbeek, C.; Sohler, W.; Fuchs, H. Second-Harmonic Imaging of Ferroelectric Domains in $LiNbO_3$ with Micron Resolution in Lateral and Axial Directions. *Appl. Phys. B: Lasers Opt.* **1998**, *67*, 593−599.
(29) Bozhevolnyi, S. I.; Hvam, J. M.; Pedersen, K.; Laurell, F.; Karlsson, H.; Skettrup, T.; Belmonte, M. Second-harmonic Imaging of Ferroelectric Domain Walls. *Appl. Phys. Lett.* **1998**, *73*, 1814−1816.
(30) Lu, Y. L.; Wei, T.; Duewer, F.; Lu, Y. Q.; Ming, N. B.; Schultz, P. G.; Xiang, X. D. Nondestructive Imaging of Dielectric-Constant Profiles and Ferroelectric Domains with a Scanning-tip Microwave Near-field Microscope. *Science* **1997**, *276*, 2004−2006.
(31) Takahashi, K.; Kida, N.; Tonouchi, M. Terahertz Radiation by an Ultrafast Spontaneous Polarization Modulation of Multiferroic $BiFeO_3$ Thin Films. *Phys. Rev. Lett.* **2006**, *96*, 117402-1−4.
(32) Sotome, M.; Kida, N.; Horiuchi, S.; Okamoto, H. Visualization of Ferroelectric Domains in a Hydrogen-Bonded Molecular Crystal using Emission of Terahertz Radiation. *Appl. Phys. Lett.* **2014**, *105*, 041101-1−6.
(33) Kinoshita, Y.; Kida, N.; Sotome, M.; Takeda, R.; Abe, N.; Saito, M.; Arima, T.; Okamoto, H. Visualization of Ferroelectric Domains in Boracite using Emission of Terahertz Radiation. *Jpn. J. Appl. Phys.* **2014**, *53*, 09PD08-1−5.
(34) Horiuchi, S.; Tokura, Y. Organic Ferroelectrics. *Nat. Mater.* **2008**, *7*, 357−366.
(35) Horiuchi, S.; Tokunaga, Y.; Giovannetti, G.; Picozzi, S.; Itoh, H.; Shimano, R.; Kumai, R.; Tokura, Y. Above-room-temperature Ferroelectricity in a Single-component Molecular Crystal. *Nature* **2010**, *463*, 789−792.
(36) Horiuchi, S.; Kumai, R.; Tokura, Y. Hydrogen-bonding Molecular Chains for High-Temperature Ferroelectricity. *Adv. Mater.* **2011**, *23*, 2098−2103.
(37) Kagawa, F.; Horiuchi, S.; Minami, N.; Ishibashi, S.; Kobayashi, K.; Kumai, R.; Murakami, Y.; Tokura, Y. Polarization Switching Ability Dependent on Multidomaintopology in a Uniaxial Organic Ferroelectric. *Nano Lett.* **2014**, *14*, 239−243.
(38) Van Aken, B. B.; Rivera, J. P.; Schmid, H.; Fiebig, M. Anisotropy of Antiferromagnetic 180° Domains in $LiCoPO_4$ and $LiNiPO_4$. *Phys. Rev. Lett.* **2008**, *101*, 157202−1−4.
(39) Horiuchi, S.; Kumai, R.; Tokura, Y. A Supramolecular Ferroelectric Realized by Collective Proton Transfer. *Angew. Chem., Int. Ed.* **2007**, *46*, 3497−3501.
(40) Sotome, M.; Kida, N.; Takeda, R.; Okamoto, H. Terahertz Radiation Induced by Coherent Phonon Generation via Impulsive Stimulated Raman Scattering in Paratellurite. *Phys. Rev. A: At., Mol., Opt. Phys.* **2014**, *90*, 033842-1−15.
(41) Fujioka, J.; Horiuchi, S.; Kagawa, F.; Tokura, Y. Dynamical Disorder of π-Molecular Structures Induced by Proton Dynamics in an Organic Ferroelectric Compound. *Phys. Rev. Lett.* **2009**, *102*, 197601-1−4.
(42) Tonouchi, M. Cutting-edge Terahertz Technology. *Nat. Photonics* **2007**, *1*, 97−105.
(43) Guan, W.; Kida, N.; Sotome, M.; Kinoshita, Y.; Takeda, R.; Inoue, A.; Horiuchi, S.; Okamoto, H. Terahertz Radiation by Optical Rectification in a Hydrogen-Bonded Organic Molecular Ferroelectric Crystal, 2-Phenylmalondialdehyde. *Jpn. J. Appl. Phys.* **2014**, *53*, 09PD07-1−4.
(44) Nahata, A.; Weling, A. S.; Heinz, T. F. A Wideband Coherent Terahertz Spectroscopy System using Optical Rectification and Electro-optic Sampling. *Appl. Phys. Lett.* **1996**, *69*, 2321−2323.
(45) Dougherty, T. P.; Wiederrecht, G. P.; Nelson, K. A. Impulsive Stimulated Raman Scattering Experiments in the Polariton Regime. *J. Opt. Soc. Am. B* **1992**, *9*, 2179−2189.
(46) Schneider, A.; Neis, M.; Stillhart, M.; Ruiz, B.; Khan, R. U. A; Günter, P. Generation of Terahertz Pulses Through Optical Rectification in Organic DAST Crystals: Theory and Experiment. *J. Opt. Soc. Am. B* **2006**, *23*, 1822−1835.
(47) Fujioka, J.; Horiuchi, S.; Kida, N.; Shimano, R.; Tokura, Y. Anisotropic Polarization π-Molecular Skeleton Coupled Dynamics in


DOI: 10.1021/acsphotonics.5b00351
*ACS Photonics* 2015, 2, 1373−1383

Proton-displacive Organic Ferroelectrics. *Phys. Rev. B: Condens. Matter Mater. Phys.* **2009**, *80*, 125134-1−8.
(48) Barkhausen, H. Zwei mit Hilfe der Neuen Verstärker Entdeckte. Erscheinungen. *Phys. Szk.* **1919**, *20*, 401.



DOI: 10.1021/acsphotonics.5b00351
*ACS Photonics* 2015, 2, 1373−1383